

Numerical investigation on the aerodynamic characteristics of high-speed train under turbulent crosswind

Mulugeta Biadgo Asress · Jelena Svorcan

Received: 4 March 2014/Revised: 12 July 2014/Accepted: 15 July 2014/Published online: 12 August 2014
© The Author(s) 2014. This article is published with open access at Springerlink.com

Abstract Increasing velocity combined with decreasing mass of modern high-speed trains poses a question about the influence of strong crosswinds on its aerodynamics. Strong crosswinds may affect the running stability of high-speed trains via the amplified aerodynamic forces and moments. In this study, a simulation of turbulent crosswind flows over the leading and end cars of ICE-2 high-speed train was performed at different yaw angles in static and moving ground case scenarios. Since the train aerodynamic problems are closely associated with the flows occurring around train, the flow around the train was considered as incompressible and was obtained by solving the incompressible form of the unsteady Reynolds-averaged Navier–Stokes (RANS) equations combined with the realizable k -epsilon turbulence model. Important aerodynamic coefficients such as the side force and rolling moment coefficients were calculated for yaw angles ranging from -30° to 60° and compared with the results obtained from wind tunnel test. The dependence of the flow structure on yaw angle was also presented. The nature of the flow field and its structure depicted by contours of velocity magnitude and streamline patterns along the train's cross-section were presented for different yaw angles. In addition, the pressure coefficient around the circumference of the train at different locations along its length was computed for yaw angles of 30° and 60° . The computed aerodynamic coefficient outcomes using the realizable k -epsilon turbulence

model were in good agreement with the wind tunnel data. Both the side force coefficient and rolling moment coefficients increase steadily with yaw angle till about 50° before starting to exhibit an asymptotic behavior. Contours of velocity magnitude were also computed at different cross-sections of the train along its length for different yaw angles. The result showed that magnitude of rotating vortex in the lee ward side increased with increasing yaw angle, which leads to the creation of a low-pressure region in the lee ward side of the train causing high side force and roll moment. Generally, this study shows that unsteady CFD-RANS methods combined with an appropriate turbulence model can present an important means of assessing the crucial aerodynamic forces and moments of a high-speed train under strong crosswind conditions.

Keywords Crosswind · High-speed trains · Computational fluid dynamics · Reynolds-averaged Navier–Stokes equations · k -Epsilon turbulence model · Numerical analysis

1 Introduction

Rail transport system brings enormous benefits to society by providing access and mobility that are essential for modern societies and economic growth and hence is a major form of passenger and freight transport in many countries [1]. In October 1964, the first high-speed rail in the world was put into operation with the highest speed of 210 km/h in Japan [2]. Since then, the last decades has witnessed the rapid development of high-speed rail system in many countries such as Germany (Fig. 1 shows a ICE-2 high-speed train made by Germany), France, Italy, Spain, China, and South Korea. Other emerging countries like

M. B. Asress (✉) · J. Svorcan
Department of Aeronautics, Faculty of Mechanical Engineering,
University of Belgrade, Kraljice Marije 16, Belgrade, Serbia
e-mail: mbiadgo@yahoo.com

J. Svorcan
e-mail: jsvorcan@mas.bg.ac.rs

Turkey and Brazil are also constructing high-speed rail networks to connect their major cities; some African countries such as Morocco, Algeria, and South Africa also proposed to build high-speed rail corridors in recent years.

Many of the current generation high-speed trains such as the Spanish AVE class 103, the German ICE-3, the French TGV Duplex, the South Korean KTX-II, the Chinese CHR C, and the Japanese Shinkansen E6 reach speeds of 300 km/h in regular operation. At these speeds, aerodynamic forces and moments are becoming more and more important for the running performance of the train. Strong crosswind may affect the running stability and riding comfort of the vehicles.

The increases of the aerodynamic forces and moments due to crosswinds may deteriorate the train operating safety and cause the train to overturn. The stability of trains in crosswinds is of concern to a number of countries with high-speed rail networks [3]. Crosswind stability of rail vehicles has been a research topic during the last decades, mainly motivated by overturning accidents. Some crosswind-related accidents are shown in Fig. 2 [4, 5]. There have been 29 wind-induced accidents of vehicles since transport service was started in 1872 in Japan. Most of these accidents happened on narrow gage (1,067 mm) lines [6]. Therefore, understanding of crosswind stability for rail vehicles has to be a topic of recognized safety issues in the railway community of every country. Recently, the aerodynamics of a train under the influence of crosswinds has been taken as a safety relevant topic and covered in national standards of UK [7], Italy [8], and Germany [9], as well as in the European Community legislation and norm [10, 11] (Fig. 3).

The risk of crosswind-induced overturning depends on both the line infrastructure and vehicles' aerodynamic characteristics [12]. On the infrastructure side, sites with tall viaducts and high embankments call for attention. The combination of modern light weight and high speed leads to an increased concern regarding the stability



Fig. 1 ICE-2 high-speed train

of high-speed trains, especially when traveling on high embankments exposed to crosswinds and sudden, powerful wind gusts. Therefore, acquiring detailed and correct data on these scenarios is quite important due to the involved risks of accidents such as a train overturning.



Fig. 2 Crosswind related accidents in Austria in 2002 (a) and Switzerland in 2007 (b) [3, 4]

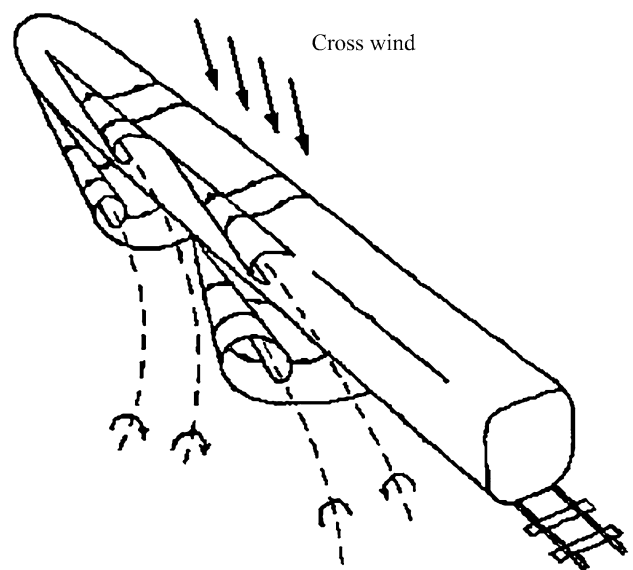


Fig. 3 Flow behind a train in a crosswind

On the vehicles side, the topic of train overturning due to crosswind exposure is closely linked to the crosswind sensitivity of the leading car of the train set, which is often the most sensitive part. This is because the front end of a railway car is usually subjected to the largest aerodynamic loads per unit length [13, 14].

The crosswind stability against overturning is a major design criterion for high speed railway vehicles and has been an experimental and/or numerical research topic for a number of scholars [15–22]. The experimental study allows to have a higher confidence in the absolute values of the measured aerodynamic forces where the numerical calculations allow to obtain a more detailed information of the flow field around the vehicle.

Among the experimental investigators, Orellano and Schober [18] have conducted a wind tunnel experiments on the aerodynamic performance of a generic high-speed train. The wind tunnel model used was a simplified 1:10 scaled ICE-2 train with and without simplified bogies. The model is known as aerodynamic train model (ATM). The study was confined to the aerodynamic loads on the stationary first car of the ATM for flat ground scenario, when exposed to yaw angles ranging from -30° to 60° . The flow speed was 70 m/s, which corresponds to Reynolds numbers of 1.4×10^6 based on the approximate model width of the train (0.3 m). In this experiment, the results have been presented through aerodynamic coefficients.

The objective of this study is to conduct a numerical investigation using unsteady Reynolds-averaged Navier–Stokes (RANS) method combined with the k -epsilon turbulence model on the aerodynamic characteristics of the leading and end cars of ICE-2 high-speed train subjected to a crosswind in static and moving ground case scenarios. The width, length, and height of the modeled train are 3.0, 29.3, and 3.9 m, respectively. For the static ground case, the numerical simulation scenario consists of a stationary train model exposed to a constant crosswind of 70 m/s at different yaw angles ranging from -30° to 60° in a similar way to the wind tunnel test performed by Orellano and Schober [18]. For the moving ground case, the numerical simulation scenario consists of a moving train exposed to effective crosswind (relative wind speed) of 70 m/s at different yaw angles ranging from -30° to 60° . The results were compared to the wind tunnel experimental data.

At present, feasible modeling technologies for turbulent flows are steady and unsteady RANS methods, large eddy simulation (LES), and detached eddy simulation (DES). Because of its relatively low computational cost, the unsteady RANS method was used in the simulations of this study. The aim is to assess the predicting capability of the unsteady RANS method by examining the behavior of the vehicle’s aerodynamic coefficients numerically and comparing to the wind tunnel results.

2 Governing equations

The equations which govern the flow over the train are the continuity and Navier–Stokes equations [23–25]. The flow around the train in our particular problem is assumed to be incompressible. Hence, for turbulent flow, the incompressible unsteady RANS equations can be written as

$$\frac{\partial \bar{u}_i}{\partial x_i} = 0, \tag{1}$$

$$\frac{\partial \bar{u}_i}{\partial t} + \bar{u}_j \frac{\partial \bar{u}_i}{\partial x_j} = -\frac{1}{\rho} \frac{\partial \bar{p}_i}{\partial x_i} + \frac{\partial}{\partial x_j} \left(\mu \frac{\partial \bar{u}_i}{\partial x_j} - \overline{\rho u'_i u'_j} \right), \tag{2}$$

where \bar{u} and \bar{p} represent the mean (time averaged) velocity and pressure, respectively; ρ is the density of air, μ is the molecular viscosity, and the last nonlinear term $\overline{u'_i u'_j}$ is the turbulent stress tensor.

2.1 Turbulence model

To model the turbulent stress tensor, the last nonlinear term in Eq. (2) and hence provide closure of the above open set of governing equations, the realizable k -epsilon turbulence model [26, 27] is used in our particular problem.

The k -epsilon model takes mainly into consideration how the turbulent kinetic energy is affected. In this model, turbulent viscosity is modeled as $\mu_t = \rho C_\mu k^2/\epsilon$, where C_μ is the eddy viscosity coefficient, k is the turbulent kinetic energy, and ϵ is the rate of dissipation of turbulent kinetic energy. The realizable k -epsilon model has been widely used in various types of flow simulation. The transport equations for realizable k -epsilon model can be expressed as follows:

$$\frac{\partial k}{\partial t} + \rho \bar{u}_j \frac{\partial k}{\partial x_j} = \frac{\partial}{\partial x_j} \left(\left(\mu + \frac{\mu_t}{\sigma_k} \right) \frac{\partial k}{\partial x_j} \right) + P_k - \rho \epsilon, \tag{3}$$

$$\begin{aligned} \rho \frac{\partial \epsilon}{\partial t} + \rho \bar{u}_j \frac{\partial \epsilon}{\partial x_j} &= \frac{\partial}{\partial x_j} \left(\left(\mu + \frac{\mu_t}{\sigma_\epsilon} \right) \frac{\partial \epsilon}{\partial x_j} \right) + \rho C_1 S \epsilon \\ &\quad - \rho C_2 \frac{\epsilon^2}{k + \sqrt{\nu \epsilon}}, \end{aligned} \tag{4}$$

$$P_k = -\rho \overline{u'_i u'_j} \frac{\partial \bar{u}_i}{\partial x_j}, \quad C_1 = \max \left(0.43, \frac{\eta}{\eta + 5} \right), \quad \eta = S \frac{k}{\epsilon}, \tag{5}$$

$$S = \sqrt{2S_{i,j}S_{i,j}}, \quad S_{i,j} = \frac{1}{2} \left(\frac{\partial \bar{u}_j}{\partial x_i} + \frac{\partial \bar{u}_i}{\partial x_j} \right). \tag{6}$$

In these equations, P_k represents the generation of turbulence kinetic energy due to the mean velocity gradients; μ and μ_t represent the molecular viscosity and eddy (turbulent) viscosity, respectively; S is the modulus of the mean rate-of-strain tensor; ν denotes the kinematic viscosity; σ_k , σ_ϵ , and C_2 are model constants with default value of 1.0, 1.2, and 1.9, respectively.

The terms on left hand side of Eqs. (3) and (4) present the local rate of change of k and ε and transport of k and ε by convection, respectively. Whereas, the terms on the right hand side present the transport of k and ε by diffusion, rate of production of k and ε , and rate of destruction of k and ε , respectively.

2.2 Atmospheric boundary layer

According to Robinson and Baker [28], when a train moves, the inclusion of an atmospheric boundary layer (ABL) simulation is necessary for producing accurate flow physics. That is when the train moves, simulation of ABL is required. In particular, the train motion induces a skewed oncoming crosswind velocity profile (see Fig. 4). For the k -epsilon model, the vertical profiles for the mean wind speed \bar{u} , turbulent kinetic energy k , and turbulence dissipation rate ε in the ABL can be expressed as follows:

$$\bar{u}(z) = \frac{u^*}{\kappa} \ln\left(\frac{z+z_0}{z_0}\right), k(z) = \frac{u^{*3}}{\sqrt{C_\mu}}, \varepsilon(z) = \frac{u^{*3}}{(z+z_0)}, \tag{7}$$

$$u^* = \kappa u_{ref} \left(\frac{z_{ref} + z_0}{z_0}\right), \tag{8}$$

where z is the height above the ground, z_0 is aerodynamic roughness length (ground roughness), u^* is the ABL friction velocity, κ is the von Karman constant, C_μ is a model constant of the realizable k -epsilon model, and u_{ref} is the reference velocity measured at the reference height z_{ref} . In the implementation of the wind alarm system, u_{ref} would be the wind speed measured at the nearest weather station at a railway line. These profiles given in Eq. (7) are commonly used as inlet profiles for computational fluid dynamics (CFD) simulations, when measured profiles are not available.

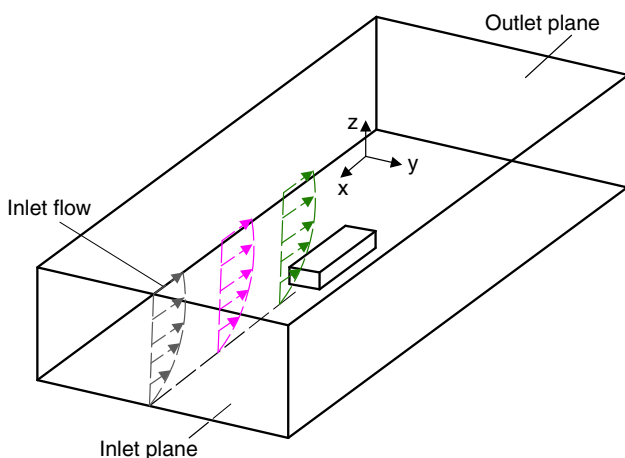


Fig. 4 Computational domain with a train model for CFD simulation

3 Numerical simulation method

The experimental investigation by Orellano and Schober [18] was done only for a stationary train model on the flat ground influenced by a constant crosswind of 70 m/s at different yaw angles. However, in this paper, the numerical simulation scenario consists of static and moving trains exposed to a crosswind at different yaw angles. In a similar fashion to the experimental set up, the numerical simulation for static ground case scenario consists of a stationary train exposed to a constant crosswind of 70 m/s at different yaw angles ranging from -30° to 60° . When a crosswind of speed V_w impinges on a train of speed V_{tr} , the yaw angle β , the prevailing wind angle α , and the resultant relative wind speed V_{rel} are as shown in Fig. 5.

On the other hand, to simulate the moving train, it is possible to consider the train static and move the ground with a speed of the train in opposite direction ($-V_{tr}$). In the moving case, a relative wind speed (effective crosswind speed) was set to be 70 m/s for all yaw angles considered. Then, the speed of the vehicle was determined for each yaw angle using the relative wind speed. Once the speed of the vehicle was known, the motion of the ground was simulated by presetting the longitudinal velocity component to the speed of travel. The Reynolds number based on the effective crosswind speed, and the width of train model is 1.4×10^7 . The commercial CFD software FLUENT was used for the numerical simulations.

According to the coordinate system given in Fig. 5, the non-dimensionalized aerodynamic side force coefficient (C_s) and rolling moment coefficient (C_{mx}) can be calculated as follows:

$$C_s = \frac{F_y}{0.5\rho u_{rel}^2 A}, \tag{9}$$

$$C_{mx} = \frac{M_x}{0.5\rho u_{rel}^2 AL}, \tag{10}$$

where F_y is the force in the y direction, M_x is the moment about x -axis, ρ is the air density, u_{rel} denotes the

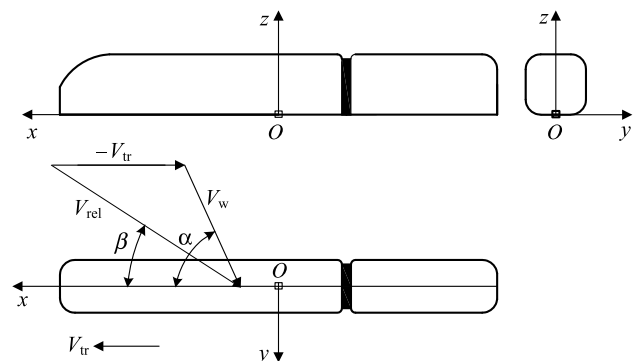


Fig. 5 Definition of yaw angle (β)

approaching air speed, A represents a fixed reference area, and L represents a fixed reference length.

3.1 Description of model geometry

Real trains are often not used for aerodynamic studies owing to their geometrical complexities; instead, simplified, shortened models are used. Performing numerical simulation for a complete train with a length of about 205 m requires more advanced computational resources than those available. In addition, since the flow structure downstream of a certain distance from the nose of the train (less than one coach length) is more or less constant, a decrease in length does not alter the essential physical features of the flow [29].

The model studied in this work is a more realistic version of the ICE-2 high-speed train which consists of the leading car, an end car, and inter car gap. The model geometry has total length of 29.3 m, width of 3 m, and height of 3.9 m. The model has been created without bogies as shown in Fig. 6. The moment reference point is set to be located at ground level in the midway of the train length. The coefficients for the aerodynamic forces and moments have been obtained using a fixed reference area of 11.6 m^2 which corresponds to the cross-sectional area of the train model, and reference length of 3 m which presents the width of the train model.

3.2 Computational domain and mesh

After the basic shape of the train has been created, a parallelepiped computational domain (see Fig. 4) with height of 50 m, width of 100 m, and length of 150 m is created for the numerical wind tunnel. In the computational domain, the model can be rotated about the z -axis by the required yaw angle for simulation. The distance between nose of vehicle and the inlet boundary is around 50 m, which is large enough to ensure that the velocity and pressure fields are uniform at the inlet and to allow the flow to develop by the time it reaches the train. The model is also sufficiently far from the top and side walls to minimize

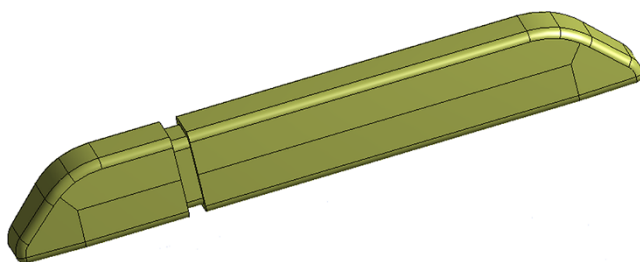


Fig. 6 Leading and end car model without bogies used in the numerical simulation

near wall effects. The clearance between the train and the flat ground (the computational domain floor) is set to be 0.15 times the height of the train.

The mesh of the computational domain was generated using a tetrahedron patch conforming method. Mesh refinement has been done on the train surfaces and surrounding areas. The generated mesh consists of about 3 million elements. The mesh resolution at the wall is very important and needs to be quantified. For standard or non-equilibrium wall functions, each wall-adjacent cell's centroid should be located within the log-law layer, $30 < y^+ < 300$. In the generated meshes, five prismatic cell layers of constant thickness were made on the train walls, and the first cell adjacent to the walls of the train was adjusted to meet the requirements of y^+ . The cross-section of the meshes with refinement on the modeled train surfaces and surrounding areas are shown in Fig. 7.

3.3 Boundary condition

For stationary case, the flow enters the domain with a uniform velocity of 70 m/s. No-slip boundary conditions were used on the train surface and the ground floor. For moving case, a relative wind speed (effective crosswind speed) of 70 m/s was used as velocity inlet. The Reynolds number based on the effective crosswind speed and the width of train model is 1.4×10^7 . Symmetry boundary conditions were used on the top and side walls. On the outlet, a homogeneous Neumann boundary condition is applied, meaning that the pressure gradient equal to zero. This will let the flow pass through the outlet without affecting the upstream flow, provided that the upstream distance to the aerodynamic body is large enough. No-slip boundary conditions were used on the train surface and the ground floor. The realizable k -epsilon model was adapted for the turbulence closure. The inflow turbulence intensity and length scale were set to be 3 % and 0.3 m, respectively. On the ground and solid surfaces, the non-equilibrium wall functions were used to determine the boundary turbulence quantities. All runs were performed in a transient mode with a time step of 0.08 s. The conventional

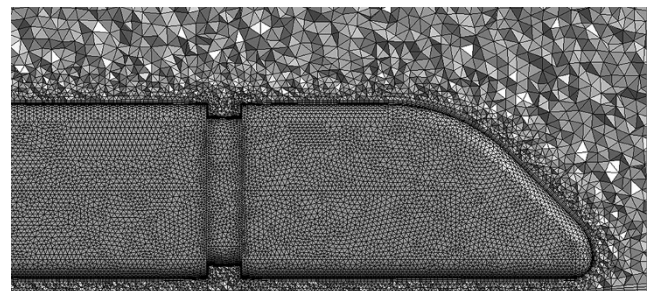


Fig. 7 Cross-section of the mesh showing elements

SIMPLE algorithm was used to solve the coupled equations, where several iterations are performed in each time step to ensure convergence.

4 Results and discussions

The computed mean force and rolling moment coefficients were compared with experimental data and shown in Figs. 8 and 9, respectively. As can be seen in the graphs, the computed side force and rolling moment coefficients are in good agreement with the experimental data. However, at yaw angles of 50° and 60°, CFD slightly over-predicts the rolling moment. This may be due to the effect of end car and inter car gap that was included in the CFD model.

The nature of the flow field and its structure are depicted by contours of velocity magnitude and streamline patterns along the train's cross-section are presented in Figs. 10, 11, 12, and 13. As expected, for large yaw angles, large flow separation zone exists on the leeward side of the train. The pressure coefficient (C_p) around the circumference of the train at different locations along its length is plotted in Figs. 14 and 16.

4.1 Side force coefficient

As can be seen from Fig. 8, the side force coefficient increases steadily with yaw angle till about 50° before it starts to exhibit an asymptotic behavior. For both cases, the computed side force coefficients are in a good agreement with the experiment. Side force is mainly caused by the pressure difference on the two sides of the train. The side force increases the wheel-track load on the leeward side

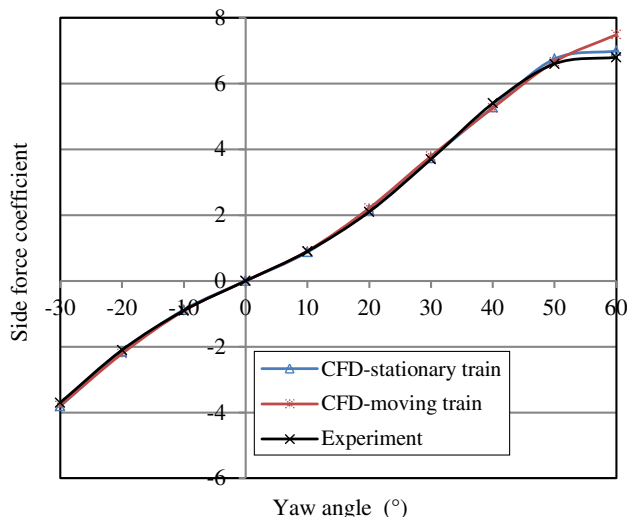


Fig. 8 Side force coefficient versus yaw angle

and the wheel-rail contact force. Large side forces worsen the wear of the wheel and rail, and may cause train derailment, or even overturning.

4.2 Rolling moment coefficient

As can be seen from Fig. 9, the rolling moment coefficient varies in a similar fashion to the side force, and the results are in a good agreement with the experiment for both cases for lower yaw angles. However, at yaw angles of 50° and 60° CFD slightly over-predicts the rolling moment. This may be due to the effect of lift force and inter car gap that was included in the CFD model. The rolling moment is the result of both the lift and side forces with the side force being the main contributor. The rolling moment is responsible for the overloading of wheel-track on the leeward side and is found to be one of the most important aerodynamic coefficients regarding crosswind stability.

4.3 Flow structure

The flow structure for different yaw angles is shown in detail by the two-dimensional streamlines at different locations along the train length (see Figs. 10, 11). As can be seen from Figs. 10 and 11, on the lower and upper leeward edges of the train, a vortex is generated and grows steadily in the axial direction. This is in agreement with Fig. 3. The vortex distribution depends on the yaw angle. An increase in the yaw angle results in an advance of the formation and breakdown of vortex. Generally, the recirculation region caused by the vortex flow starts being adjacent to the walls of the train, and then it slowly drifts away from the surface as the flow develops further toward

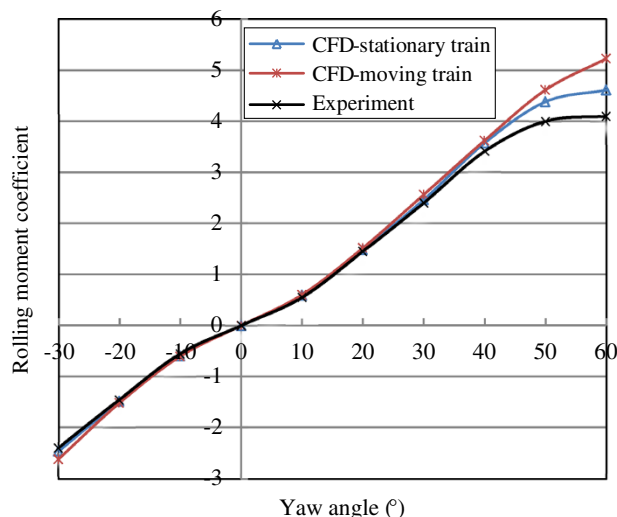


Fig. 9 Rolling moment coefficient versus yaw angle

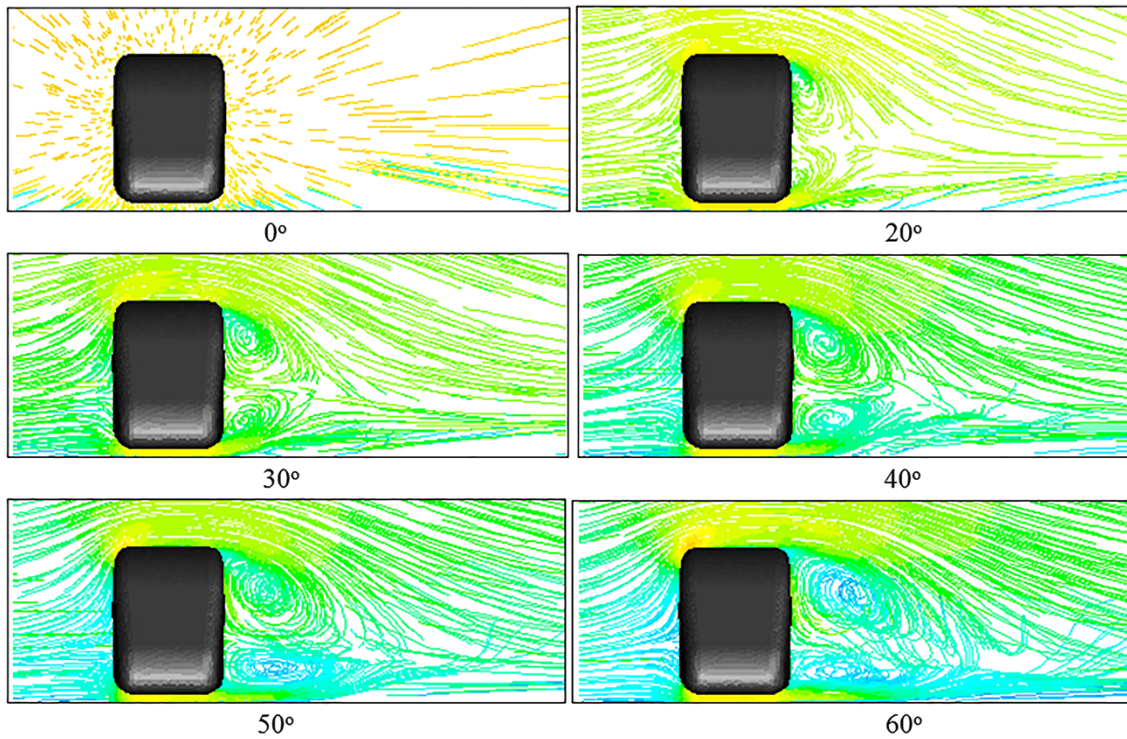


Fig. 10 Streamlines along the train’s cross-section at 6 m from the nose of the train

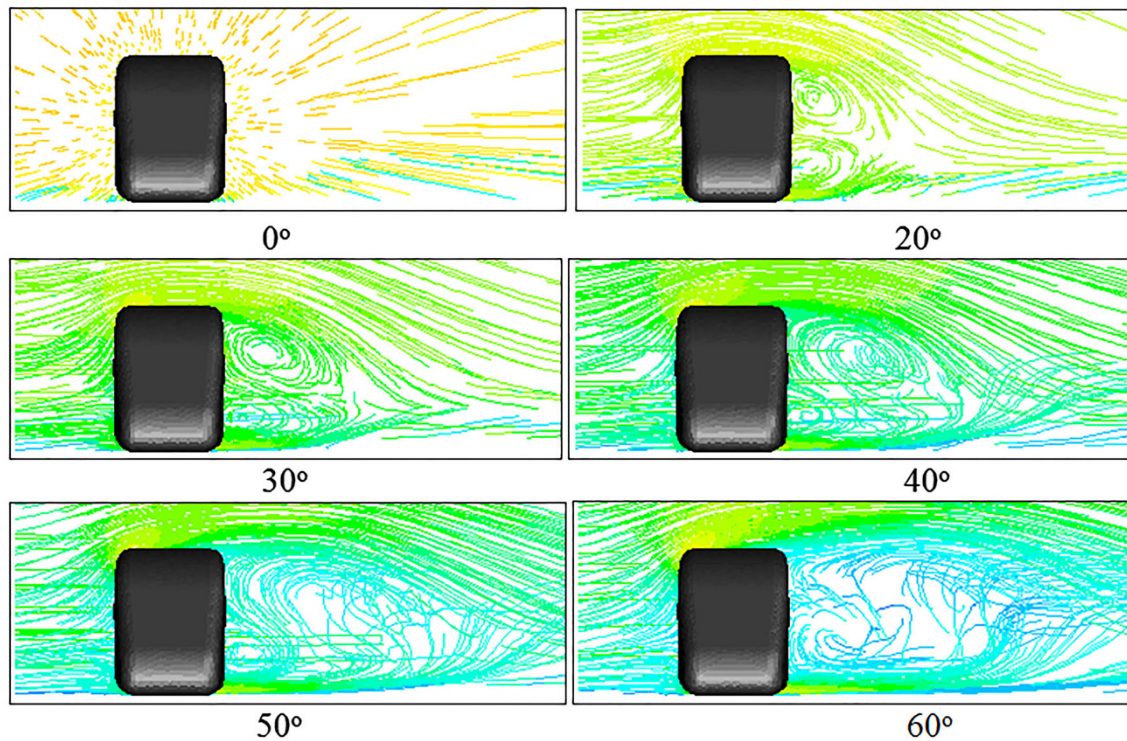


Fig. 11 Streamlines along the train’s cross-section at 14 m from the nose of the train

the wake. The flow separation takes place on both the lower and upper leeward edges. The pressure coefficient around the circumference of the train at different

locations along its length has been computed for yaw angles of 30° and 60° and is shown in Figs. 14, 15, and 16. Obviously, the pressure distribution on the surface

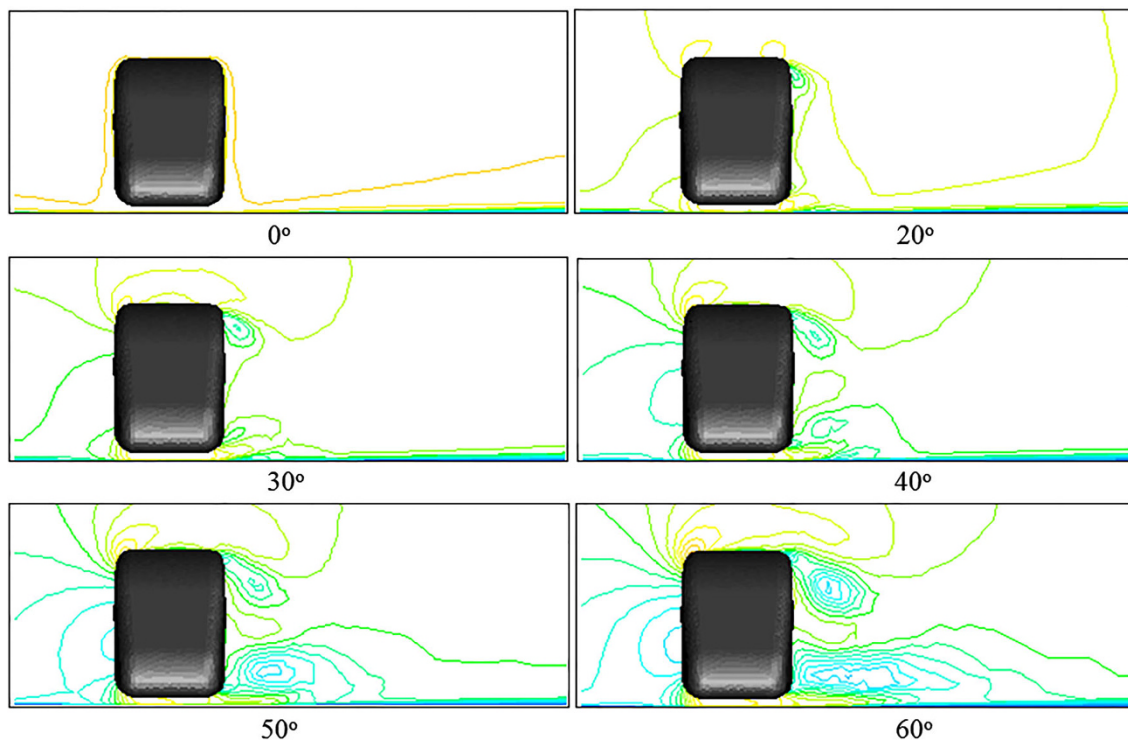


Fig. 12 Contours of velocity magnitude along the train's cross-section at 6 m from the nose of the train

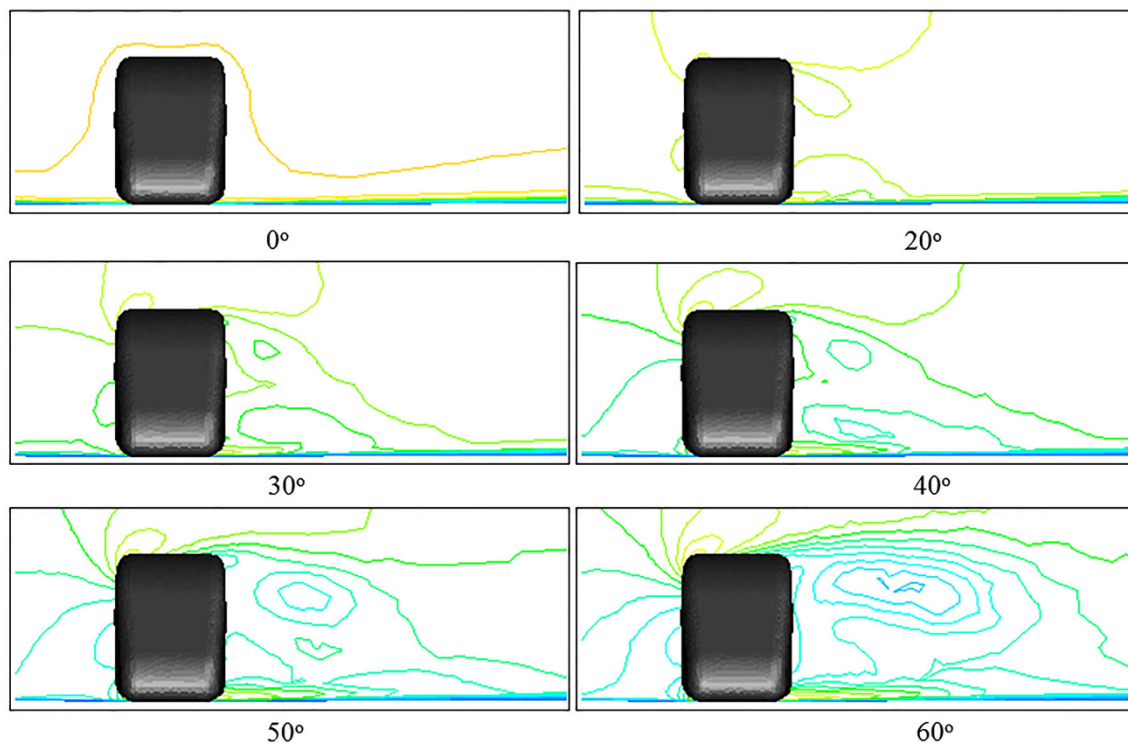


Fig. 13 Contours of velocity magnitude along the train's cross-section at 14 m from the nose of the train

depends on the yaw angle. However, it does not change much along the train length except in a small region close to the nose as can be seen from Figs. 14 and 15. This

shows that the pressure distribution around a high-speed train at higher yaw angles is almost independent on the axial position.

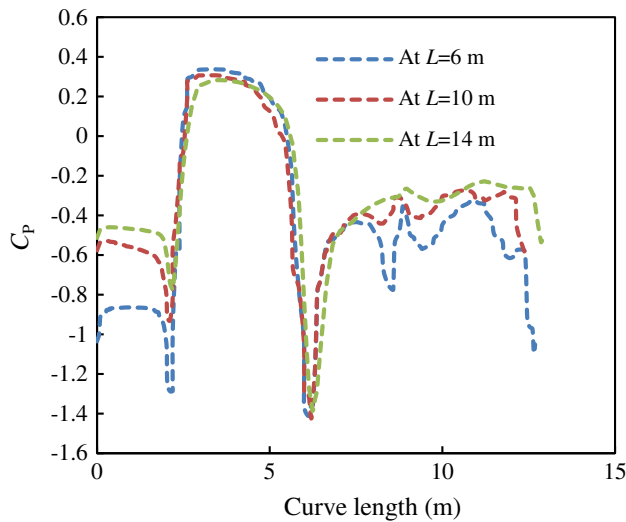


Fig. 14 Pressure coefficient along the train’s cross-section at different distance (L) from the nose of the train for yaw angle of 30°

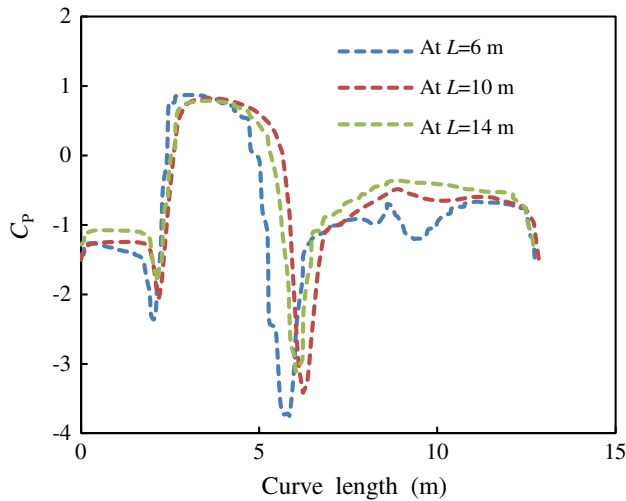


Fig. 15 Pressure coefficient along the train’s cross-section at different distance (L) from the nose of the train for yaw angle of 60°

Contours of velocity magnitude have been computed at a cross-section of 6 m and 14 m from the nose of the train along its length for different yaw angles (see Figs. 12, 13). Wind direction has greater influence on flow structure in the rear wake. As can be seen from Figs. 12 and 13, in the absence of side wind (yaw angle 0°), symmetric condition existed. For yaw angles greater than 0 degree, more vortexes evolved on leeward side. The magnitude of rotating vortex in the lee ward side increased with increasing yaw angle. This leads to the creation of a low-pressure region in the lee ward side of the train causing high side force and rolling moment.

The pressure coefficient around the circumference of the train at different locations along its length is plotted in Figs. 14 and 15 for yaw angle of 30° and 60° for static

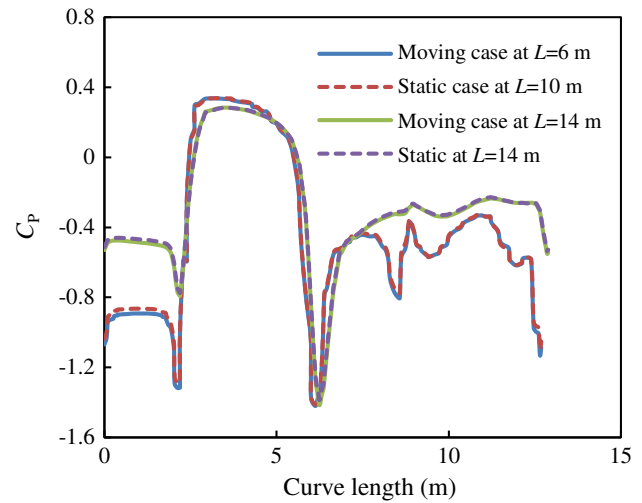


Fig. 16 Pressure coefficient along the train’s cross-section at different distance (L) from the nose of the train for yaw angle of 30°

ground case scenario. Obviously, the pressure distribution on the surface depends on the yaw angle. However, it does not change much along the train length except in a small region close to the nose (at $L = 6$ m from the nose). This shows that the pressure distribution around a high-speed train at higher yaw angles is almost independent on the axial position. Similar observations were reported in the experimental works of Robinson and Baker [28]. Figure 16 shows the pressure coefficient around the circumference of the train at different locations for both static and moving cases. As can be seen from the figure, the moving ground creates a little bit more negative pressure, which implies a little bit more lift.

5 Conclusion

The flow of turbulent crosswind over a more realistic ICE-2 high-speed train model has been simulated numerically by solving the unsteady three-dimensional RANS equations. The simulation has been done in static and moving ground case scenarios for different yaw angles ranging from -30° to 60° . The computed aerodynamic coefficient outcomes using the realizable k-epsilon turbulence model were in good agreement with the wind tunnel data. Both the side force coefficient and rolling moment coefficients increase steadily with yaw angle till about 50° before starting to exhibit an asymptotic behavior.

The nature of the flow field and its structure depict by contours of velocity magnitude and streamline patterns along the train’s cross-section has been also presented for different yaw angles. As can be seen from the stream line patterns along the train’s cross-section, on the lower and

upper leeward edges of the train a vortex is generated and grows steadily in the axial direction. An increase in the yaw angle results in an advance of the formation and breakdown of vortex on the leeward edges. Contours of velocity magnitude were also computed at different cross-sections of the train along its length for different yaw angles. The result showed that magnitude of rotating vortex in the lee ward side pronounced with increasing yaw angle which leads to the creation of a low-pressure region in the lee ward side of the train causing high side force and roll moment.

The pressure coefficient around the circumference of the train at different locations along its length has been computed for yaw angles of 30° and 60°. Obviously, the pressure distribution on the surface depends on the yaw angle. However, it does not change much along the train length except in a small region close to the nose. This shows that the pressure distribution around a high-speed train at higher yaw angles is almost independent on the axial position.

Generally, this study shows that unsteady CFD-RANS methods combined with an appropriate turbulence model can present an important means of assessing the crucial aerodynamic forces and moments of a high-speed train under strong crosswind conditions. Since the observed variations between some of the CFD and wind tunnel results may be due to the turbulence parameters such as turbulence intensity and length scale; study on the influence of those parameters using advanced modeling like LES is vital. The aerodynamic data obtained from this study can be used for comparison with future studies such as the influence of turbulent crosswinds on the aerodynamic coefficients of high-speed train moving in dangerous scenarios such as high embankments.

Open Access This article is distributed under the terms of the Creative Commons Attribution License which permits any use, distribution, and reproduction in any medium, provided the original author(s) and the source are credited.

References

1. EuDaly K, Schafer M, Boyd J, Jessup S, McBridge A, Glischinski S (2009) The complete book of north American railroading. Voyageur Press, Stillwater, pp 1–352
2. Zhou L, Shen Z (2011) Progress in high-speed train technology around the world. *J Mod Transp* 19(1):1–6
3. Baker CJ (2004) Measurements of the cross wind forces on trains. *J Wind Eng Ind Aerodyn* 92:547–563
4. Peters J-L (1990) How to reduce the cross wind sensitivity of trains. Siemens Transportation Systems, Muenchen
5. Thomas D (2009) Lateral stability of high-speed trains at unsteady crosswind. licentiate Thesis in Railway Technology, Stockholm, Sweden
6. Suzuki M, Tanemoto K, Maeda T (2003) Aerodynamic characteristics of train/vehicles under cross winds. *J Wind Eng Ind Aerodyn* 91:209–218
7. Blakeney A (2000) Resistance of railway vehicles to roll-over in gales. Railway group standard, Safety & Standards Directorate, Railtrack PLC, London
8. Mancini G, Cheli R, Roberti R, Diana G, Cheli F, Tomasini G (2003) Cross-wind aerodynamic forces on rail vehicles wind tunnel experimental tests and numerical dynamic analysis. In: The proceedings of the World congress on railway research, Edinburgh
9. DB Netz AG (2006) Richtlinie 80704 Aerodynamik/Seitenwind, Frankfurt
10. EC (2006) TSI-technical specification for interoperability of the trans-European high speed rail system. Eur Law, Off J Eur Commun
11. CEN (2010) EN 14067-6: railway applications Aerodynamics Part 6: requirements and test procedures for crosswind assessment. European Committee for Standardization, Brussels
12. Elisa M, Hoefener L (ed.) (2008) Aerodynamics in the open air (AOA). WP2 Cross Wind Issues, Final Report, DeuFraKo Project, Paris
13. Diedrichs B (2008) Aerodynamic calculations of cross wind stability of a high-speed train using control volumes of arbitrary polyhedral shape. In the VI international colloquium on: bluff bodies aerodynamics & applications (BBAA), Milan
14. Carrarini A (2007) Reliability based analysis of the crosswind stability of railway vehicles. *J Wind Eng Ind Aerodyn* 95:493–509
15. Kwon H, Park Y-W, Lee D, Kim M-S (2001) Wind tunnel experiments on Korean high-speed trains using various ground simulation techniques. *J Wind Eng Ind Aerodyn* 89:1179–1195
16. Baker CJ (2002) The wind tunnel determination of crosswind forces and moments on a high speed train. In: Notes on numerical fluid mechanics, Vol. 79, Springer-Verlag, Berlin, p 46–60
17. Boccione M, Cheli F, Corradi R, Diana G, Tomasini G (2003) Wind tunnel tests for the identification of the aerodynamic forces on rail vehicles. In: the XI ICWE-international conference on wind engineering, Lubbock
18. Orellano A, Schober M (2006) Aerodynamic performance of a typical high-speed train. In: The proceedings of the 4th WSEAS international conference on fluid mechanics and aerodynamics, Elounda
19. Cheli F, Corradi R, Rocchi D, Tomasini G, Maestrini E (2008) Wind tunnel test on train scaled models to investigate the effect of infrastructure scenario. In: The VI international colloquium on: bluff bodies aerodynamics & applications (BBAA), Milan
20. Cheli F, Ripamonti F, Rocchi D, Tomasini G (2010) Aerodynamic behavior investigation of the new EMUV250 train to cross wind. *J Wind Eng Ind Aerodyn* 98:189–201
21. Krajnovic S, Ringqvist P, Nakade K, Basara B (2012) Large eddy simulation of the flow around a simplified train moving through a crosswind flow. *J Wind Eng Ind Aerodyn* 110:86–99
22. Guilmineau E, Chikhaoui O, Deng G, Visonneau M (2013) Cross wind effects on a simplified car model by a DES approach. *Comput Fluids* 78:29–40
23. Wendt JF (2009) Computational Fluid Mechanics: an Introduction. Springer-Verlag, Berlin
24. Currie IG (1974) Fundamental mechanics of fluids. McGraw-Hill, New York
25. Blazek J (2001) Computational fluid dynamics: principles and applications. Elsevier Science Ltd, Oxford
26. Wilcox DC (2006) Turbulence modelling for CFD, 3rd edn. DCW Industries, Inc, la Canada
27. Schlichting H, Gersten K (1999) Boundary layer theory. Springer-Verlag, New York
28. Robinson CG, Baker CJ (1990) The effect of atmospheric turbulence on trains. *J Wind Eng Ind Aerodyn* 34:251–272
29. Khier W, Breuer M, Durst F (2000) Flow structure around trains under side wind conditions: a numerical study. *Comput Fluids* 29:179–195